Design and Demodulation of a Fiber-Optic Fabry-Perot Sensor Applied in a High-Frequency Pneumatic System

Jianli Yang , Qian Yang, Shengchao Chen , *Student Member, IEEE*, Sufen Ren , Guanjun Wang ,
and Mengxing Huang

Abstract—This study proposes a high-frequency pneumatic system and demodulation method based on polydimethylsiloxane (PDMS) film-embedded fiber-optic Fabry-Perot sensor to meet the conflicting requirements of small sizes and wide frequency-response range not achieved by conventional pneumatic probes. The high modulus of elasticity of PDMS films provides the potential for an upper limit of a pneumatic frequency response up to 20 kHz, and the new demodulation algorithm, based on the ability of the F-P cavity to return to its initial length from the maximum cavity length change, is utilized to analyze its variation. The process of recovering F-P cavity corresponds with the sparse part of the signal, which takes advantage of the unique characteristics of interference fringes in this part. Moreover, the relationship between the relative change of the F-P cavity length and pneumatic pressure, as well as the relationship between the duration of the relative change of the F-P cavity length and the frequency are analyzed comprehensively. The rationality of the proposed demodulation scheme is verified from the angle-error analyses. These analyses could be helpful for integrated and high-frequency response pneumatic detection.

Index Terms—Fabry-Perot cavity, fiber-optic, high-frequency, interference fringe, pneumatic.

I. INTRODUCTION

TURBOMACHINERY is a key power device that supports national energy, basic industries, and propulsion technology. This device plays a significant role in generators, gas turbines, and aerospace engines [1]. In previous studies, scientists have improved the overall efficiency of turbomachinery used in experiments by optimizing its structure [2]. Majority of these studies are based on time-averaged data, implying that the airflow field is in a steady state [3]. However, the actual turbomachinery's airflow field is unsteady and can be resolved into three-dimensional-vector components [4], [5]. Unsteadiness in the turbomachinery airflow fields typically results in at least 25% efficiency losses when compared to steady-state conditions [6], [7]. Therefore, pneumatic measurements are necessary for understanding the airflow field within a turbomachine and ultimately improving the overall machine efficiency [8].

Existing pneumatic measurement technology can be divided into two categories: contact and non-contact measurements [9]. For contact measurements, pneumatic and hot-wire probes are employed [10]. These types of probes are easy to design, and they have a good stability and high signal-to-noise ratio, but their size affects the airflow field [11]. Non-contact measurements are difficult to perform in narrow spaces due to the system complexity, causing inconveniences such as optical access difficulty and difficulty in particle-tracking near the wall. Hence, the majority of these systems are currently employed only in laboratories [12], [13].

As a conventional, accurate, and economical flow field measurement tool, pneumatic probes are widely employed in flow field studies. There are three commonly used types of pneumatic probes [14], [15], [16]: three-hole, five-hole, and seven-hole probes. With the development of gas turbines, aero-engines, and other high-speed flow devices, the demand for dynamic flow field measurements is increasing. The frequency of the flow field can reach 20 kHz or even more than 100 kHz [17], such as an aero-engine, which requires a pneumatic probe that can measure high-frequency flow. Furthermore, shrinking the size of the probe is critical for reducing airflow disturbance and increasing the measurement accuracy. However, current commercial sensors used for flow field measurements cannot meet all the aforementioned requirements [18]. For example, the Kulite-XCQ-062 commercial sensor is insensitive to signals exceeding 20 kHz, and its film diameter is 1.7 mm. Therefore, designing a miniaturize-sized pneumatic probe that adapts to high-frequency environments is important.

Jianli Yang, Qian Yang, Shengchao Chen, Sufen Ren, and Mengxing Huang are with the State Key Laboratory of Marine Resource Utilization in South China Sea, and School of Information and Communication Engineering, Hainan University, Haikou 570228, China (e-mail: jianleeyang@hainanu.edu.cn; iamyangqianw@126.com; chenschao820@163.com; aug_0815@163.com; huangmx09@hainanu.edu.cn).

Guanjun Wang is with the State Key Laboratory of Marine Resource Utilization in South China Sea, and School of Information and Communication Engineering, Hainan University, Haikou 570228, China, and also with the Wuhan National Laboratory for Optoelectronics, Huazhong University of Science and Technology, Wuhan 430074, China (e-mail: wangguanjun@hainanu.edu.cn).
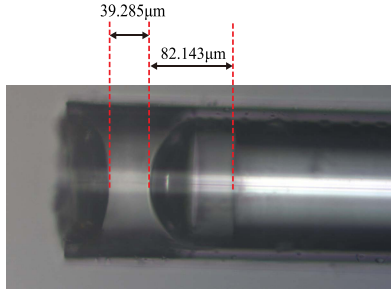
Fig. 1. Fabry-Perot sensor structure diagram.

Recently, advanced sensors have been proposed, but the fiber-optic Fabry-Perot (F-P) sensor has attracted most attention due to its advantages of sensitivity to high-frequency signals and being easy to miniaturize. The high modulus of elasticity of a PDMS film-embedded fiber-optic F-P sensor provides the sensor with the potential to achieve a 20 kHz frequency response; its film diameter can be made as small as 128 μm, this frequency response measurement will be implemented in future work. Wang [19] used a diaphragm-embedded fiber-optic sensor sensitive to frequencies of 15 kHz to detect an acoustic signal. Zhang [20] manufactured a similar sensor, and its signal-to-noise ratio reached 31.22 dB with an ultrasonic excitation pulse of 300 kHz. In addition to the aforementioned advantages, the fiber-optic F-P sensor has an excellent stability, and it can replace the conventional pneumatic probe in strong electromagnetic-interference- and high-temperature environments.

To resolve the issues related with conventional pneumatic probes, this study is the first to propose a high-frequency pneumatic system and demodulation method based on PDMS film-embedded fiber-optic Fabry-Perot sensor; the proposed system has the advantages of sensitivity to high-frequency signals and being small-sized for high-frequency flow field measurements. Additionally, experiments were conducted to compare the commercial sensor with the proposed system. The new demodulation method was proposed to analyze the spare part of the signal, which refers to a sinusoidal signal with a gradually increasing period. Demodulation results revealed the relationship between the relative cavity-length variation and air pressure, as well as the relationship between the relative cavity-length variation duration and frequency. Finally, the error of the signal demodulation is analyzed to demonstrate the rationality of the demodulation scheme.

II. SENSING AND DEMODULATION THEORY

The structure of the fiber-optic F-P sensor adopted in this study is shown in Fig. 1, with a cavity length of 82.143 μm and film thickness of 39.285 μm. The measurement of pneumatic signals employed F-P sensors with different cavity lengths and PDMS film thicknesses, which revealed that the signals measured with PDMS film thicknesses around 40 μm and F-P cavity lengths around 80 μm were the most observable. Its specific manufacturing process is as follows: A PDMS film is coated on the end of a glass tube with an inner diameter of 128 μm and outer diameter of 200 μm. Then, a thin fiber of 125 μm diameter
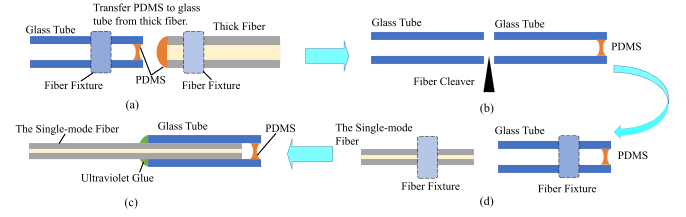

Fig. 2. F-P cavity-sensor production process: (a) Dip a thick fiber of 200 μm diameter into the PDMS glue to coat its end with a small amount of the glue, and then fix the thick fiber and the glass tube on the optical platform, the PDMS glue was coated onto the end of the glass tube by adjusting the position of the glass tube to touch the end of thick fiber end with PDMS glue. (b) Cut off the glass tube about 15 mm. (c) Fix a thin fiber of 125 μm diameter on the optical platform, and adjust its position to insert through the glass tube. (d) Finally, fix the thin fiber with Ultraviolet glue.
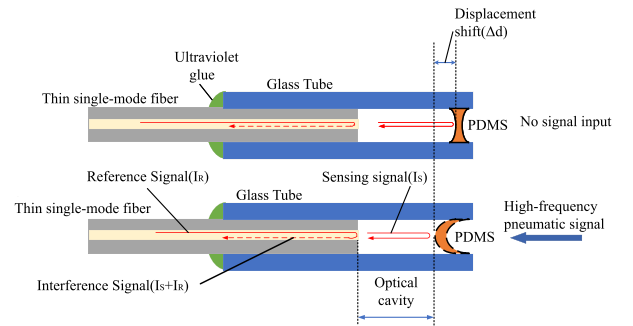

Fig. 3. F-P sensor measurement principle.

is inserted through the other end of the glass tube. Finally, the thin fiber is fixed with ultraviolet glue. The specific fabrication process of the fiber-optic F-P sensor structure is shown in Fig. 2 and can also be found in [21].

The resonant frequency of the sensor determines the maximum frequency that the fiber-optic sensor can measure [22]. According to a rule of thumb for the resonant pressure sensor, the maximum frequency of the signal is 0.2 of the resonant frequency of the sensor. The formula for calculating the resonant frequency is

$$f_{00} = \frac{\alpha_{00}}{4\pi} \left[\frac{E}{3\omega(1-\mu^2)} \right]^{1/2} \left[\frac{h}{(d/2)^2} \right], \qquad (1)$$

where f_{00} is the lowest resonant frequency; α_{00} is a constant related to the vibrating modes, which is 10.21 for the lowest natural frequency; E is Young's modulus and μ is the Poisson ratio; ω is the mass density of the material; and r and h are the radius and the thickness of the diaphragm, respectively. Since the material of the diaphragm is silicon dioxide, Young's modulus, the Poisson ratio and the mass density are chosen. Therefore, the theoretical resonant frequency was calculated to 11.15 MHz, which allows capturing the maximum theoretical frequency of the signal up to 2.2 MHz.

The principle of the F-P sensor in high-frequency pneumatic signal measurements is illustrated in Fig. 3. Due to the low reflectivity of the fiber end and PDMS film, the multi-beam interference generated by the fiber F-P cavity can be approximated to a double-beam interference [23], [24]. At the end of the fiber, approximately 4% of the input light (reference signal) will
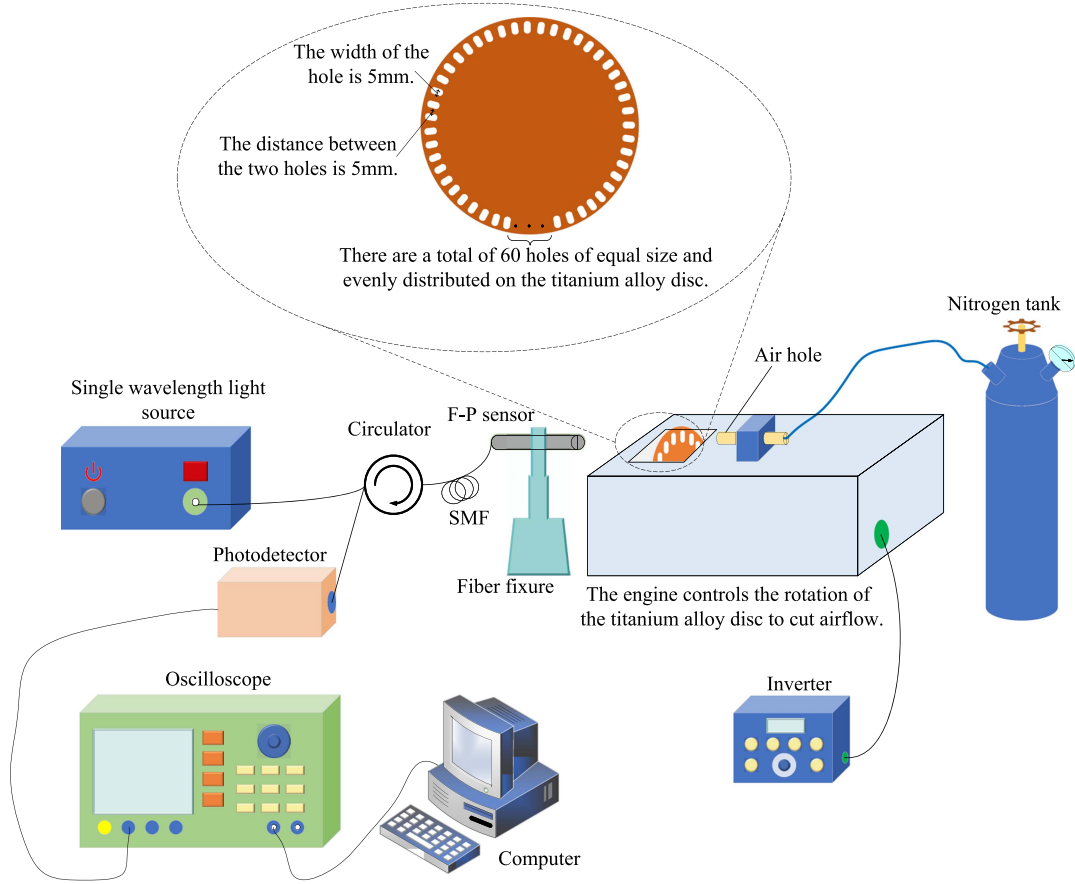
Fig. 4. Experimental measurement system.

be reflected back [25]. The other 96% is transmitted to the F-P cavity and reflected on the PDMS film [26], which is transmitted back to the fiber (sensing signal). The two aforementioned beams will form a series of interference fringes [27]. With various frequencies and air pressures, the PDMS film will generate an elastic deformation corresponding to the dynamic F-P cavity-length change [28], [29], [30]. Therefore, frequency and pressure information can be obtained from the interference fringes.

The interference signal obtained from the fiber is mathematically described by

$$I = I_S + I_R + 2\sqrt{I_S I_R} \cos \varphi, \qquad (2)$$

where I_R represents the intensity of the reference signal and I_S represents the intensity of the sensing signal. φ corresponds to the optical phase shift, and it is a function of the relative cavity variation (Δd) [31], expressed as

$$\varphi = \frac{4\pi \cdot n \cdot \Delta d}{\lambda}, \qquad (3)$$

with n being the refractive index of the optical cavity, and λ the wavelength of the interrogation light.

In Eq. (2), let $A = I_R + I_S, B = 2\sqrt{I_R I_S}$, where A is the interference constant term, and B represents the amplitude of the interference term [32]. Then, Eq. (2) is written as

$$I = A + B \cos \varphi, \qquad (4)$$

By shifting the terms of the aforementioned equation, φ can be derived as

$$\varphi = \arccos \frac{I - A}{B}, \qquad (5)$$

where Δd is the variable of the F-P cavity length as a function of time t, and combining Eqs. (3) and (5), we can acquire Δd by measuring the interference light intensity [33]. The domain of definition of Eq. (5) is in the range $[-1, 1]$. If the interference light intensity I exceeds this range, the solution can be obtained in segments.

III. EXPERIMENTAL SETUP

The F-P system designed for high-frequency pneumatic signal measurements is illustrated in Fig. 4. The experimental setup contains two parts, one is the signal measurement and the other is the pneumatic part. A single-wavelength laser of wavelength 1550 nm is employed by the signal measurement part. As shown in Fig. 5, the F-P sensor employed in the experiment has the largest slope and is the most sensitive at 1550 nm. And according to the laboratory conditions, only a single wavelength light source of 1550 nm is available. The emitted light wave spreads through an optical circulator to the F-P sensor, which is held by the fixture. The interference signal is transmitted back to the photodetector through the circulator and is concurrently displayed on an oscilloscope. Furthermore, these data are transferred to
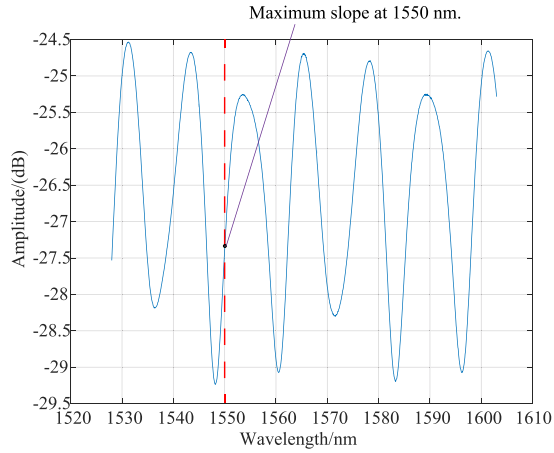
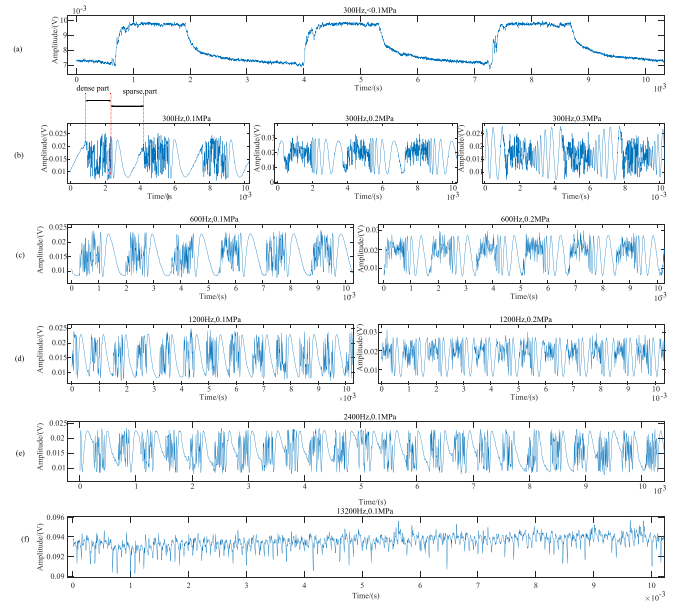Fig. 5.   Spectrum of the F-P sensor employed in the experiment.

Fig. 6.   Outputs from simulating the pneumatic high-frequency module: (a)–(f) are the measurements using F-P sensors for different air pressures and HVFs.

the computer for processing using Eq. (5). In the pneumatic part, a motor revolving a titanium-alloy disc is integrated into an alloy box, and the holes of the disc are exposed outside the case to cut airflow. There are 60 holes evenly distributed along the circumference of the disc, and the width of each hole and the distance between two adjacent holes are equals to 5 mm. Therefore, the hole vibration frequency (HVF) is 60 times the disc frequency (DF). Furthermore, the motor controlled by an inverter rotates the disc at various frequencies. The air pressure (All air pressure in the text refers to gauge pressure.) is controlled by adjusting the nitrogen tank's valve. The magnitude of the air pressure value can be obtained from the barometer. The airflow travels through the air hole fixed on top of the box.

The interference spectrum of the F-P sensor used in this experiment is shown in Fig. 5. Multiple interference fringes can be seen in the figure, and its light intensity is at least 3 db, which led to an apparent waveform on the oscilloscope.

The measurement system is designed to acquire the air pressure and HVF from the interference signal. In this experiment, the interference signal of the following HVF and air pressure data were measured: HVF was 300 Hz with 0.1, 0.2, and 0.3 MPa air pressures; HVF was 600 Hz with 0.1 and 0.2 MPa air pressures; HVF was 1.2 kHz with 0.1 MPa and 0.2 MPa air pressures. Finally, HVF was 2.4 kHz with a 0.1 MPa air pressure. The interference signal under the 0.1 MPa air pressure was also obtained. These measurements were then repeated with a commercial sensor.

IV. EXPERIMENTAL RESULTS AND DISCUSSION

In this section, we will discuss the results measured by the F-P sensor and its demodulation and the F-P sensor demodulation error. The commercial-sensor measurements and analysis are presented in the final subsection.

A. F-P Sensor Measurements and Demodulation

The F-P sensor measurement results are summarized in Fig. 6, which displays a 0–10 ms waveform. As is apparent from Fig. 6, the interference signal frequency is consistent with the HVF.

The signal is approximately a square wave for air pressures less than 0.1 MPa. When the air pressure is greater than or equal to 0.1 MPa, the signal becomes complicated because a cycle is separated into sparse and dense parts (as shown in Fig. 6(b)). The sparse part and the dense part will be described in detail next paragraph. The sparse part is a sinusoidal signal with a gradually increasing period, whereas the dense part is not easily recognized. Owing to the F-P cavity variation exceeding half of the laser wavelength (refer to Eq. (3)), the signals in Fig. 6(b)– (e) display multiple peaks and valleys during a cycle, which corresponds to the bright and dark fringes. Additionally, there are no multiple peaks and valleys in Fig. 6(a) owing to low air pressure, implying that the F-P cavity variation does not exceed half of the laser wavelength. The data measured at a frequency of 13.2 KHz for the pneumatic signal are shown in Fig. 6(f). The large frequency of the signal leads to more noise components in the signal, and the PDMS film layer will vibrate with the airflow, which makes the signal amplitude unstable and inconvenient for demodulation. The demodulation approach proposed in this study is applied to the data in Fig. 6(b)–(e).

The airflow travels from the air hole to the sensor, leading to the signal waveform becoming dense. Because the cavity length varies rapidly, a dense sine wave with high frequency and short period will be observed. When the cavity variation reaches the maximum, the signal is presented as a constant. Additionally, when the disc revolves to a position without an air hole to block the airflow, the F-P cavity begins recovering its original length. However, the rate of cavity-length variation is slower than when the gas is blown, and its recovery rate gradually decreases, which develops the sparse part. Subsequently, the disc rotates to the air hole position again, the air flow almost instantaneously causes the F-P relative cavity variation to reach its maximum. With the disc revolving, the F-P cavity length will repeat the aforementioned changes.
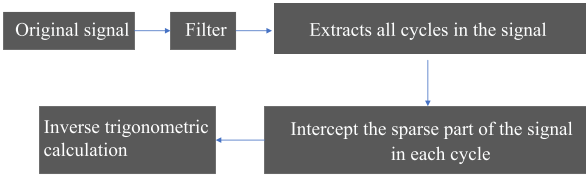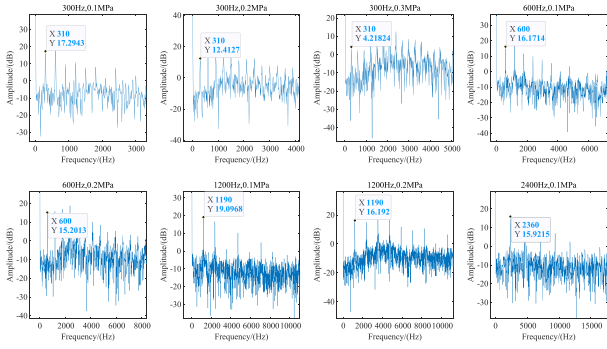
Fig. 7. Signal-demodulation process.

Fig. 8. Signal Fast Fourier Transform results.

Fig. 9. Signal extraction.

As the air pressure exceeds 0.1 MPa, the signal cycle is divided into sparse and dense parts, which contain interference information. However, as the film is made of PDMS, the dense part causes considerable noise, as shown in Fig. 6. When the airflow blows to the F-P sensor resulting in the maximum membrane deformation, the PDMS film will vibrate with the airflow. If the vibration is beyond half of the laser wavelength, the interference signal will develop bright and dark fringes. This leads to dense peaks and valleys in a cycle, resulting in noise that hinders demodulation. Additionally, if the vibration does not surpass half of the laser wavelength, the amplitude of the dense part will fluctuate slightly. Therefore, the sparse part is selected for demodulation owing to its apparent peaks and valleys. The method focuses on the recovery of the F-P cavity from the maximum cavity length to the initial cavity length; the demodulation result is relative cavity variation. Therefore, the demodulated relative cavity length is the length of recovery of the F-P cavity from the maximum cavity length to the initial cavity length. As the disc rotates, it is possible that the F-P cavity may not have regained its initial length before the gas has been blown through the air hole to the sensor, at which point the demodulated relative cavity length variation is not the maximum.

When the air pressure increases, the sparse part possesses more peaks and valleys, as shown in Fig. 6(b)–(e), which is attributed to the increase of the F-P cavity variation leading to bright and dark fringe increments. Additionally, the frequency of the signal can be acquired by by subjecting the signal to an FFT transform, the details of which are shown in Fig. 8. Fig. 8 is the spectrum derived from the fast Fourier transform of the data in Fig. 6(b)–(e). The first frequency component in each graph is the pneumatic signal frequency, and the maximum error in frequency is no more than 5%.

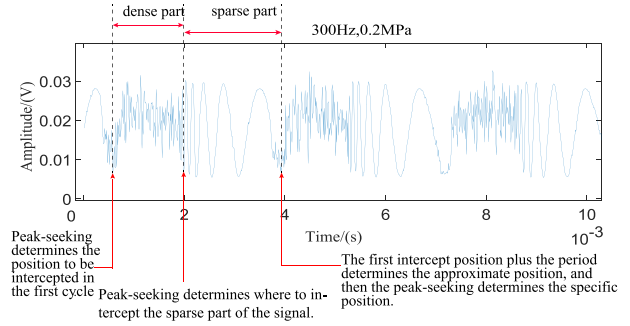The demodulation flow is indicated in Fig. 7. High frequencies and air-pressure levels cause a larger noise amplitude, which interferes with the signal. Therefore, the noise amplitudes have to be filtered. After filtering, each cycle in the signal, which includes the sparse and dense parts, is intercepted. Because the peaks and valleys in the sparse part are more detectable, the peak-seeking algorithm searches near the sparse and dense parts boundaries, starting from the sparse part; it selects a location near the boundary as the first interception position. As the signal period is conveniently available, the next approximate interception position is calculated by adding the period to the former interception location. Subsequently, the peak-seeking algorithm is applied in the vicinity of this location to determine the interception position, by which all cycles are captured from the signal. The sparse part is then extracted from each period. At the boundaries of the dense and sparse portions, the transition from the dense to sparse part is presented as a constant to a sine wave with a high frequency, indicating that the frequency abruptly varies from zero to a large value. The frequency of the sine wave signal increases sharply from the sparse to the dense part. Each cycle is extracted in a dense—sparse sequence from the signal, as demonstrated in Fig. 9. Two approaches to intercept the sparse part of the period are available: 1. Determine the interception location from the signal frequency variation, which is transformed from a constant to a large value. 2. Select the peak or valley from a sparse part that is near the boundary of the sparse and dense portions as the interception position.

Since the Fiber-Optic F-P sensor is fabricated with PDMS material, the membrane layer will vibrate with the airflow, leading to the dense part of signal being complicated. The traditional intensity demodulation method is not suitable for the dense part of the signal, and this method has requirements for the variation range of the cavity length, which does not apply to the demodulation of high-frequency pneumatic signals. The proposed demodulation method focuses on the recovery of the F-P cavity from the maximum cavity length to the initial cavity length; and the demodulation result is relative cavity variation. The process of recovering F-P cavity corresponds with the sparse part of the signal, which takes advantage of the obvious characteristics of interference fringes in this part.

We consider a 0.2 MPa, 300 Hz HVF signal as an example, and analyze the signal in terms of wavelet time and frequency with Amor wavelet. The time–frequency analysis is illustrated in Fig. 10. Fig. 10(a) is the pseudo-color image, and (b) illustrates the three-dimensional time–frequency analysis. According to
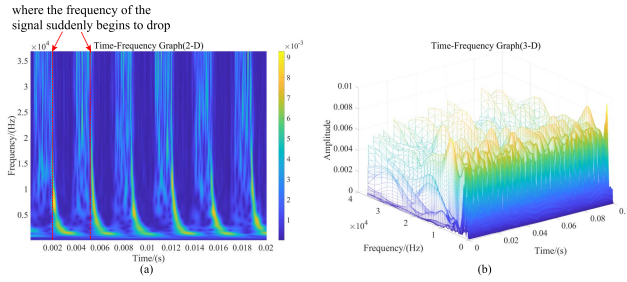
Fig. 10. Time and frequency analysis of the output from a 0.2 MPa, 300 Hz pneumatic signal: (a) two-dimensional time-frequency analysis; (b) three-dimensional time-frequency analysis.
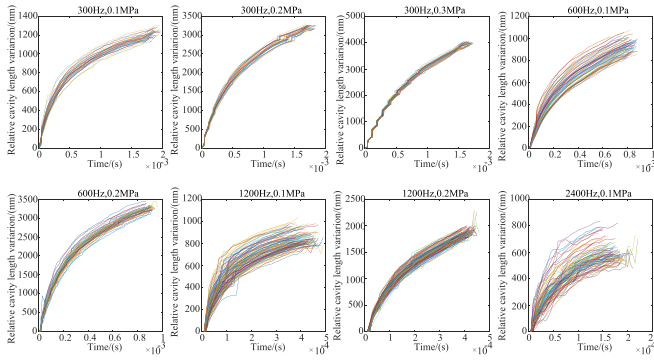

Fig. 11. Demodulation of the sparse parts of all periods in the signal at different air pressures and HVFs.
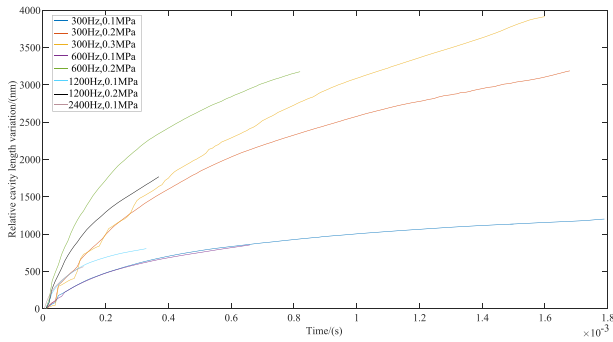

Fig. 12. Relative cavity length variation for different air pressure levels and HVFs.

the figure, the period of the signal is 3 ms; the location of the frequency's abrupt change is also obtained. Before intercepting the sparse parts, the signal is filtered again to further remove the noise influence. Completing the aforementioned steps, the signal is processed using inverse trigonometry according to Eq. (5).

The demodulations, which analyze the sparse part of all periods in the signals at different air pressures and HVFs, are illustrated in Fig. 11. Eight curves are plotted by averaging all the curves in each diagram of Fig. 11, displayed in Fig. 12. The demodulated relative cavity length is the length of recovery of the F-P cavity from the maximum cavity length to the initial cavity length. For easy observation, the demodulated relative cavity lengths are represented as monotonically increasing in the first quadrant.
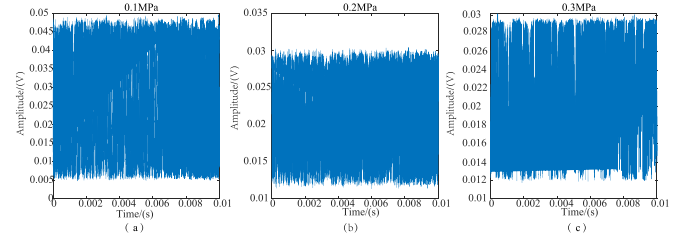

Fig. 13. Verification of the dithering of the film layer: (a)–(c) are the signals measured from the F-P sensor using the airflow of different pressures with the disk stationary.

According to Fig. 11, the consistency of the demodulation results improves with increasing air pressure and deteriorates with increasing HVF. The detailed factors are analyzed as follows: The relative cavity length variation and number of interference fringes increase with the increase in air pressure, leading to an increase in the amount of demodulated data and optimization of the consistency of demodulation. As the HVF increases, the noise frequency components turn more complex, and the smaller-signal period results in the number of extracted sparse parts and demodulated curves increasing, deteriorating the demodulation consistency. When the airflow blows to the F-P sensor resulting in the maximum membrane deformation, the PDMS film will vibrate with the airflow. As the HVF increases, the PDMS film layer may even vibrate during the recovery from the maximum F-P cavity length to the initial cavity length, which results in fluctuations in the demodulated cavity length. In addition, the demodulation method requires intercepting the sparse part of the signal, which may result in over-intercepting or under-intercepting one cycle when the signal fluctuates greatly.

As illustrated in Fig. 12, the HVF is acquired from the duration of the relative cavity length variation, whereas the air pressure is obtained from the maximum cavity variation of each curve. The relative cavity variation increases with increasing air pressure; the value is maximum at 0.3 MPa, followed by the value at 0.2 MPa, and is the smallest at 0.1 MPa. As the HVF increases from long to short (300 Hz, 600 Hz, 1200 Hz, 2400 Hz), the duration of the relative cavity variation decreases. Additionally, the air pressure increases leading to a high relative cavity variation rate.

B. F-P Sensor Demodulation Error Analysis

1) Dithering of PDMS Film Layers: The experiment employs an extrinsic fiber-optic F-P sensor structure, with PDMS embedded as a film layer. Airflow blows to the sensor, leading to film jittering during deformation; when the film reaches its deformation maximum it will still dither. If the dithering exceeds half of the laser wavelength, the interference signal will develop bright and dark fringes, which result in dense peaks and valleys in a cycle. The specific waveforms can be seen in Fig. 6. To verify the membrane-layer jittering, the airflow of various pressure levels is applied to the sensor, with the air hole facing directly to the sensor and the disc remaining stationary. The experimental results are illustrated in Fig. 13. The cavity length
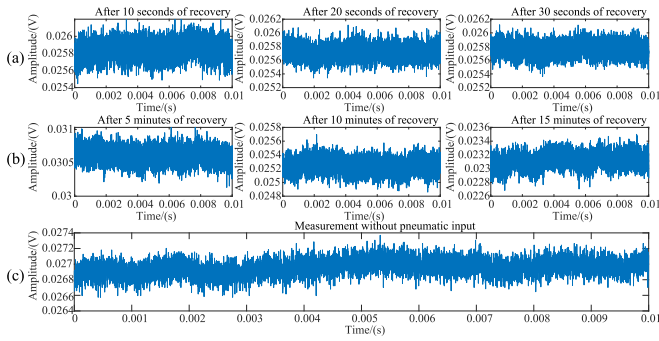
Fig. 14. Examination of the repeatability of the F-P sensor: (a)–(c) are the results of the PDMS film recovery at different times after switching off the pneumatic part.

Fig. 15. Algorithm error.

variation increases as the air pressure increases; however, the signal amplitude does not necessarily increase with the cavity length variation. Eq. (4) demonstrates that the amplitude of the signal varies sinusoidally with the cavity length and is not proportional to it. In Fig. 13, the signal amplitudes should have been a constant; however, owing to the PDMS-film dithering, they fluctuate, which resembles noise.

2) Repeatability of the Structure: To examine the ability of the F-P sensor to reproduce the same results, the following experiment was implemented: The signal was measured when air pressure and HVF were zero, as shown in Fig. 14(c). After applying 0.1 MPa air pressure and 300 Hz HVF to the measurement system, the nitrogen tank and motor were immediately switched off. The signal was recorded after various times, as illustrated in Fig. 14(a)–(b). Comparison of these signals with the signal amplitudes in Fig. 14(c) leads to the following conclusions: The recovery of the membrane layer is slow, with minimal change during the first 30 s. Several minutes later, the membrane layer moved toward the initial position; it did not recover to the initial position after 15 min, indicating the poor repeatability of the structure. We intend to subsequently adopt other materials instead of PDMS to resolve this issue.

3) Algorithm Error: The demodulation scheme in the experiment targets the sparse part of the signal. However, errors occur while extracting the sparse part. To intercept the sparse part from each cycle, it is necessary to determine the boundary between the sparse and dense parts. The boundary is determined with a peak-seeking algorithm. However, the signal is complicated in the dense part due to the dithering of the membrane layer; therefore, the algorithm might over-count or under-count a wave peak or valley while determining the boundary, resulting in demodulated results with an error of half the wavelength of the laser, as demonstrated in Fig. 15. When intercepting the sparse parts of all cycles, only a small portion of the data will be in error; this portion is much smaller than the normal data, and the error can be decreased by averaging the demodulation results.

C. Commercial Sensor Measurements and Analysis

The commercial sensor measurements are illustrated in Fig. 16. As shown in Fig. 7, noise interference still exists in the measurements taken using commercial sensors. This is mainly
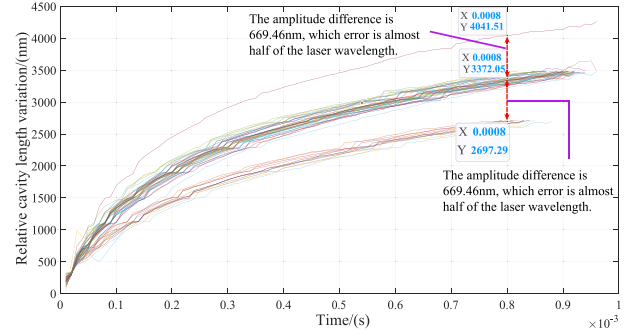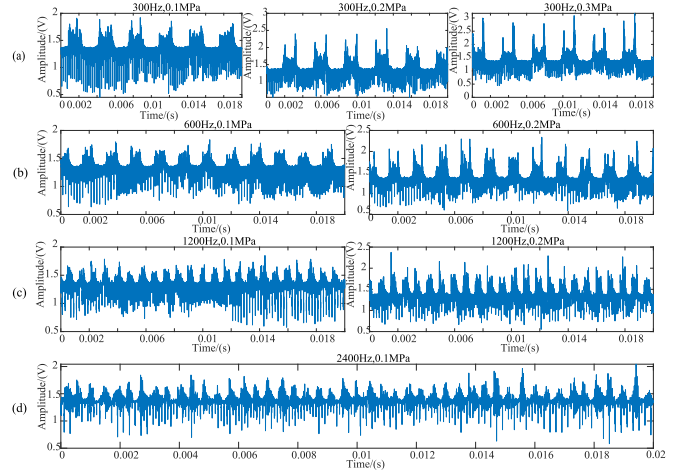

Fig. 16. Outputs from simulating the pneumatic high-frequency module: (a)–(e) are the measurements obtained using commercial sensors for different air pressures and HVF.
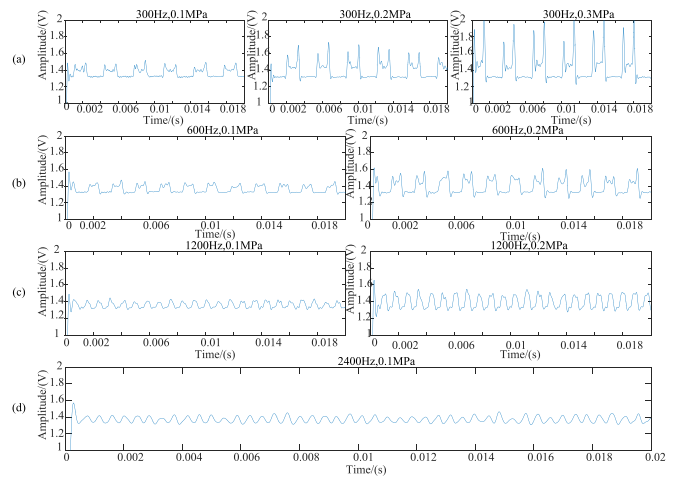
Fig. 17. (a)–(d) results showing the filtered measurements from commercial sensors.

attributed to the following two factors: 1. A commercial bridge sensor is applied to the measurement, and the pneumatic part is attached to a three-phase power, leading to a small amount of electricity in the chassis, which generates an electric field that interferes with the sensor measurements. 2. The airflow transmitted to the sensor through the air hole might be reflected to the

Fig. 18.   Commercial Sensor Signal Fast Fourier Transform results.
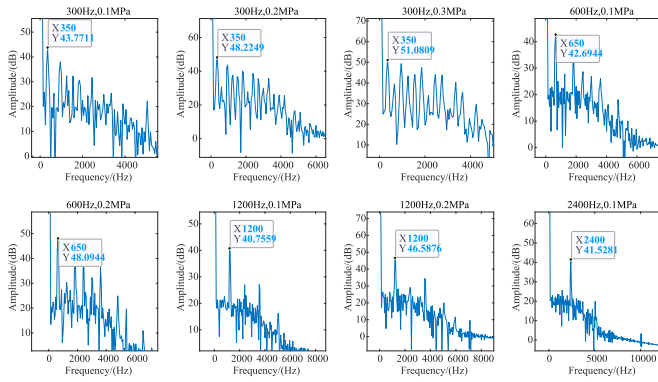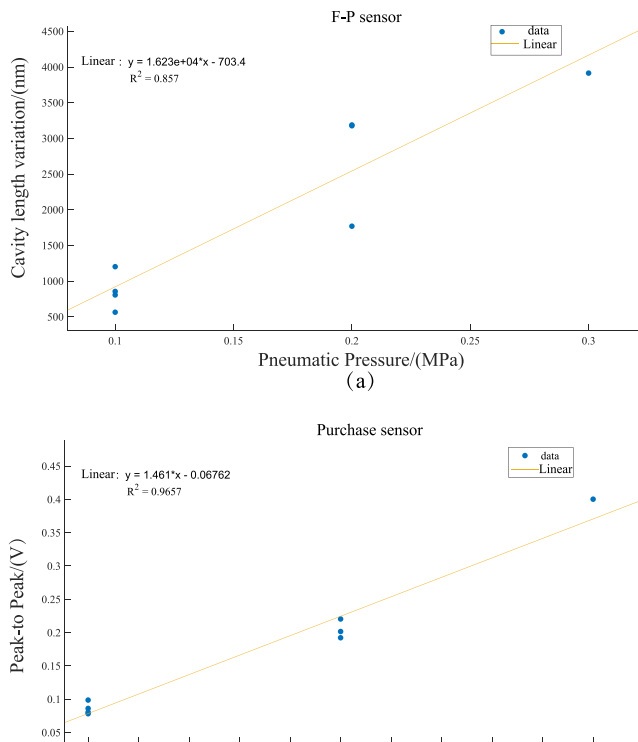

Fig. 19.   Fitting the pressure curves of F-P sensors and commercial sensors: (a) Fitting based on the data of pneumatic signal pressure versus the cavity length variation in Fig. 12. (b) Fitting based on the data of pneumatic signal pressure versus signal peak-to-peak in Fig. 17.

disc for secondary reflection, increasing the signal amplitude in the rising or falling edge. The data in Fig. 16 are filtered with a Butterworth low-pass filter, and the filtered results are summarized in Fig. 17.

As shown in Fig. 17, the signal frequency is the HVF, and the increment of air pressure results in a larger signal strength. The airflow travels from the air hole to the sensor, leading to a continuous high level in the signal, whereas the continuous low level corresponds to when the disc blocks the airflow. As the HVF increases, the signal waveform tends to be a triangular wave due to the shorter durations of the high and low levels, the signal's frequency component becomes more complex and the processed signal is less effective. This is not as intuitive as

using the F-P sensor to demodulate the relative cavity length to observe the air pressure and frequency.

The frequency of the signal is derived from the fast Fourier transform of the filtered signal, as shown in Fig. 18. The maximum frequency error measured by the commercial sensor can be up to 16.7%, which is larger than that of the F-P sensor, and the noise part of the signal is still existed in a small part.

As shown in Fig. 19, the pressure curves of the commercial sensor and the F-P sensor were fitted separately. The curve fitted by the F-P sensor was not better than that of the commercial sensor, due to the error caused by the violent vibration of the PDMS membrane layer with the airflow during the deformation process.

V. CONCLUSION

This study first combined a fiber-optic F-P cavity sensor with a pneumatic probe owing to its high sensitivity and easy miniaturization. The new demodulation approach proposed uses the relative cavity-length variation, which contains pressure and frequency information. The change in the relative cavity length increases with increase in air pressure, and the duration of the change in relative cavity length decreases with the increase in frequency. However, because PDMS with a high modulus of elasticity is used to fabricate the film layer, the film vibrates violently with the gas, causing errors during demodulation making calibration difficult. The demodulation error is approximately half of the laser wavelength, but it can be reduced by averaging the demodulation results for each cycle. The rationality of the proposed new demodulation scheme is also verified from the angle error analysis. These analyses could be helpful for integrated and high-frequency response pneumatic detection.

REFERENCES

[1] O. P. Sharma, G. F. Pickett, and R. H. Ni, "Assessment of unsteady flows in turbines," *J. Turbomachinery*, vol. 114, no. 1, pp. 79–90, 1990.

[2] D. L. Simon, S. Gang, G. W. Hunter, T. H. Guo, and K. J. Semega, "Sensor needs for control and health management of intelligent aircraft engines," in *Proc. ASME Turbo Expo 2004: Power Land, Sea, and Air*, 2004, pp. 873–882.

[3] C. Lenherr, A. I. Kalfas, and R. S. Abhari, "High temperature fast response aerodynamic probe," *J. Eng. Gas Turbines Power*, vol. 133, no. 1, pp. 11603–11603, 2010.

[4] I. Tzanakis, D. Eskin, A. Georgoulas, and D. Fytanidis, "Incubation pit analysis and calculation of the hydrodynamic impact pressure from the implosion of an acoustic cavitation bubble," *Ultrasonics Sonochemistry*, vol. 21, no. 2, pp. 866–878, 2014. [Online]. Available: https://www.sciencedirect.com/science/article/pii/S1350417713002344

[5] R. G. Dominy and H. P. Hodson, "An investigation of factors influencing the calibration of five-hole probes for three-dimensional flow measurements," *J. Turbomachinery*, vol. 115, no. 3, pp. 513–519, 1993. [Online]. Available: https://doi.org/10.1115/1.2929281

[6] J. S. Wyler, "Probe blockage effects in free jets and closed tunnels," *J. Eng. Power*, vol. 97, no. 4, pp. 509–514, 1975. [Online]. Available: https://doi.org/10.1115/1.3446046

[7] D. Lengani et al., "A method for the determination of turbulence intensity by means of a fast response pressure probe and its application in a LP turbine," *J. Thermal Sci.*, vol. 21, pp. 21–31, 2012.

[8] S. Chen et al., "Reconstruction of Fabry-Perot interferometric sensor spectrum from extremely sparse sampling points using dense neural network," *IEEE Photon. Technol. Lett.*, vol. 34, no. 24, pp. 1337–1340, Dec. 2022.

[9] L. Porreca, M. Hollenstein, A. I. Kalfas, and R. S. Abhari, "Turbulence measurements and analysis in a multistage axial turbine," *J. Propulsion Power*, vol. 23, no. 1, pp. 227–234, 2007.

[10] J. F. Brouckaert, "Fast response aerodynamic probes for measurements in turbomachines," *Proc. Inst. Mech. Eng., Part A. J. Power Energy*, vol. 221, no. 6, pp. 803–813, 2007.

[11] N. Wildmann, S. Ravi, and J. Bange, "Towards higher accuracy and better frequency response with standard multi-hole probes in turbulence measurement with remotely piloted aircraft (RPA)," *Atmospheric Meas. Techn.*, vol. 7, no. 4, pp. 1027–1041, 2014.

[12] R. W. Ainsworth, J. L. Allen, and J. J. M. Batt, "The development of fast response aerodynamic probes for flow measurements in turbomachinery," *J. Turbomachinery*, vol. 117, no. 4, pp. 625–634, 1 1995.

[13] H. J. Humm, C. R. Gossweiler, and G. Gyarmathy, "On fast-response probes: Part 2-aerodynamic probe design studies," *J. Turbomachinery*, vol. 117, no. 4, pp. 618–624, 1995.

[14] D. Delhaye, G. Paniagua, J. F. Oro, and R. Dénos, "Enhanced performance of fast-response 3-hole wedge probes for transonic flows in axial turbomachinery," *Experiments Fluids: Exp. Methods Appl. Fluid Flow*, vol. 50, no. 1, pp. 163–177, 2011.

[15] M. Mansour, N. Chokani, A. I. Kalfas, and R. S. Abhari, "Time-resolved entropy measurements using a fast response entropy probe," *Meas. Sci. Technol.*, vol. 19, no. 11, pp. 115401-1–115401-14, 2008.

[16] I. Bosdas, M. Mansour, A. I. Kalfas, and R. S. Abhari, "A fast response miniature probe for wet steam flow field measurements," *Meas. Sci. Technol.*, vol. 27, no. 12, pp. 125901-1–125901-17, 2016.

[17] I. Bosdas, M. Mansour, A. I. Kalfas, and R. S. Abhari, "An optical backscatter probe for time resolved droplet measurements in turbomachines," *Meas. Sci. Technol.*, vol. 27, no. 1, pp. 015204-1–015204-19, 2016.

[18] X. Cai et al., "Coarse water in low-pressure steam turbines," *Proc. Inst. Mech. Eng., Part A. J. Power Energy*, vol. 228, no. A2, pp. 153–167, 2014.

[19] J. Wang et al., "Diaphragm-based optical fiber sensor array for multi-point acoustic detection," *Opt. Exp.*, vol. 26, no. 19, pp. 25293–25304, Sep. 2018. [Online]. Available: http://opg.optica.org/oe/abstract.cfm?URI=oe-26-19-25293

[20] W. Zhang et al., "An optical fiber Fabry-Perot interferometric sensor based on functionalized diaphragm for ultrasound detection and imaging," *IEEE Photon. J.*, vol. 9, no. 3, Jun. 2017, Art. no. 7103208.

[21] L. Li et al., "Polydimethylsiloxane diaphragm-based fiber ultrasonic sensor with high sensitivity and wide spectrum response range," *AIP Adv.*, vol. 11, no. 7, 2021, Art. no. 075021. [Online]. Available: https://doi.org/10.1063/5.0053742

[22] N. Wu, X. Zou, Y. Tian, J. Fitek, and M. Maffeo, "An ultra-fast fiber optic pressure sensor for blast event measurements," *Meas. Sci. Technol.*, vol. 23, no. 5, 2012, Art. no. 055102.

[23] C. Macià-Sanahuja, H. Lamela, and J. A. García-Souto, "Fiber optic interferometric sensor for acoustic detection of partial discharges," *J. Opt. Technol.*, vol. 74, no. 2, pp. 122–126, Feb. 2007. [Online]. Available: http://opg.optica.org/jot/abstract.cfm?URI=jot-74-2-122

[24] S. Chen, F. Yao, S. Ren, G. Wang, and M. Huang, "Cost-effective improvement of the performance of AWG-based FBG wavelength interrogation via a cascaded neural network," *Opt. Exp.*, vol. 30, no. 5, pp. 7647–7663, Feb. 2022. [Online]. Available: http://opg.optica.org/oe/abstract.cfm?URI=oe-30-5-7647

[25] Q. Rong et al., "Ultrasonic sensitivity-improved Fabry–Perot interferometer using acoustic focusing and its application for noncontact imaging," *IEEE Photon. J.*, vol. 9, no. 3, Jun. 2017, Art. no. 6802511.

[26] S. Liang, C. Zhang, W. Lin, L. Li, and B. Lin, "Fiber-optic intrinsic distributed acoustic emission sensor for large structure health monitoring," *Opt. Lett.*, vol. 34, no. 12, pp. 1858–1860, 2009.

[27] D. H. Wang and P. G. Jia, "Fiber optic extrinsic Fabry–Perot accelerometer using laser emission frequency modulated phase generated carrier demodulation scheme," *Opt. Eng.*, vol. 52, no. 5, 2013, Art. no. 055004.

[28] L. Liu et al., "UV adhesive diaphragm-based FPI sensor for very-low-frequency acoustic sensing," *IEEE Photon. J.*, vol. 8, no. 1, Feb. 2016, Art. no. 6800709.

[29] S. Chen et al., "Fabry-Perot interferometric sensor demodulation system utilizing multi-peak wavelength tracking and neural network algorithm," *Opt. Exp.*, vol. 30, no. 14, pp. 24461–24480, Jul. 2022. [Online]. Available: http://opg.optica.org/oe/abstract.cfm?URI=oe-30-14-24461

[30] J. Ma, Y. Yu, and W. Jin, "Demodulation of diaphragm based acoustic sensor using sagnac interferometer with stable phase bias," *Opt. Exp.*, vol. 23, no. 22, pp. 29268–29278, Nov. 2015. [Online]. Available: http://opg.optica.org/oe/abstract.cfm?URI=oe-23-22-29268

[31] D. Tosi, "Simultaneous detection of multiple fiber-optic Fabry-Perot interferometry sensors with cepstrum-division multiplexing," *J. Lightw. Technol.*, vol. 34, no. 15, pp. 3622–3627, Aug. 2016.

[32] B. Liu, J. Lin, H. Liu, Y. Ma, L. Yan, and P. Jin, "Diaphragm based long cavity Fabry–Perot fiber acoustic sensor using phase generated carrier," *Opt. Commun.*, vol. 382, pp. 514–518, 2017.

[33] R. Wang, Z. Liu, and X. Qiao, "Fringe visibility enhanced Fabry-Perot interferometer and its application as gas refractometer," *Sensors Actuators B: Chem.*, vol. 234, pp. 498–502, 2016.